Atmos. Chem. Phys. Discuss., 12, 33411–33442, 2012
www.atmos-chem-phys-discuss.net/12/33411/2012/
doi:10.5194/acpd-12-33411-2012

Atmospheric Chemistry and Physics Discussions

An improved HIRS upper tropospheric water vapor dataset and its correlations with major climate indices

L. Shi[1], **C. J. Schreck III**[2], **and V. O. John**[3]

[1]National Climatic Data Center, National Oceanic and Atmospheric Administration, Asheville, North Carolina, USA
[2]Cooperative Institute for Climate and Satellites, North Carolina State University, Asheville, North Carolina, USA
[3]Met Office Hadley Centre, Exeter, UK

Received: 30 November 2012 – Accepted: 17 December 2012
– Published: 21 December 2012

Correspondence to: L. Shi (lei.shi@noaa.gov)

Published by Copernicus Publications on behalf of the European Geosciences Union.

Abstract

A new version of the upper tropospheric water vapor dataset is developed using inter-satellite calibrated all-sky High-Resolution Infrared Radiation Sounder (HIRS) data. In this dataset, the majority of pixels that do not affect the water vapor processing in the upper troposphere are retained. Compared to the previous version that was based on column-clear-sky data, the new version has a much better daily spatial coverage and provides a better representation of the atmosphere. The HIRS observation patterns are compared to microwave sounder measurements. The differences between the two types of sounders are examined, and the analysis displays that the differences vary with respect to brightness temperature. An examination of the correlations of the HIRS upper tropospheric water vapor with major climate indices shows that the dataset is well correlated with climate indices especially in cold seasons. The selected climate indices track climate variation signals covering regions from the tropics to the poles. The correlation analysis shows the potential of using the upper tropospheric water vapor dataset together with a suite of many atmospheric variables to monitor regional climate changes and locate global teleconnection patterns.

1 Introduction

With data starting in 1978, the High-Resolution Infrared Radiation Sounder (HIRS) has the longest record among satellite sounding measurements. The satellites carrying HIRS include the Television Infrared Observation Satellite (TIROS-N), the operational National Oceanic and Atmospheric Administration (NOAA) polar orbiting satellite series (hereafter abbreviated as NOAA-#, where # is the satellite number), and the Meteorological Operational Satellite Program (METOP). There are 20 channels in a HIRS instrument, among which channel 12 measures the upper tropospheric water vapor (UTWV). The measurement has facilitated numerous studies on large scale circulations and associated atmospheric systems.

ACPD
12, 33411–33442, 2012

Among these studies, Bates et al. (1996), McCarthy and Toumi (2004), and Shi and Bates (2011) showed that UTWV closely tracks the El Niño – Southern Oscillation (ENSO) evolutions. Bates and Jackson (2001) examined the strong interaction between tropical and mid-latitude planetary waves based on UTWV data. Using UTWV as one of the datasets, Sohn and Park (2010) studied tropical circulations in the past three decades. Soden et al. (2005) examined the moistening of the upper troposphere. A long-term UTWV dataset was used in the evaluation of climate model simulations (Iacono et al., 2003). The trend and variability of UTWV were analysed in various studies (Geer et al., 1999; Bates and Jackson, 2001; Bates et al., 2001; McCarthy and Toumi, 2004). These large-scale studies have been based on column-cloud-cleared data. But as the distribution of cloud frequencies ranges from ∼0.20 to ∼0.95 (Wylie et al., 2007), column-cloud-cleared data may not be representative of many weather systems. Using measurements from microwave sounders, John et al. (2011) illustrated possible limitations of clear-sky data. To expand the applications of the UTWV data, we develop a new HIRS UTWV dataset with improved sky-coverage.

2 UTWV data

For over three decades, HIRS measurements have been made from more than a dozen satellites. Due to differences in the channel spectral response functions and independence in each instrument's calibration, biases exist from satellite to satellite (Shi et al., 2008). Based on overlapping satellites' zonal averages from the equator to the poles, Shi and Bates (2011) quantified intersatellite biases on TIROS-N, NOAA satellite series, and METOP-A. These intersatellite bias corrections are applied in the present study to adjust HIRS measurements to the same base satellite (NOAA-12) as that in the previous column-clear-sky version of UTWV to form a climatologically homogenized time series.

ACPD
12, 33411–33442, 2012

2.1 Removal of upper tropospheric clouds

HIRS UTWV processing can be affected by clouds in the upper troposphere. Clouds that penetrate through the upper troposphere and tropopause are usually associated with deep convective systems characterized by very low infrared brightness temperatures, therefore cold brightness temperatures in the window channel (near 11 μm) have been commonly used in identifying penetrating clouds. When studying infrared satellite images of the oceanic warm-pool region (80° E–160° W), Mapes and Houze (1993) found that half of the very cold (< 208 K) cloudiness is contributed by cloud clusters greater than 20 000 km^2 in size, while half of the moderately cold (< 235 K) cloudiness is contributed by cloud clusters greater than 100 000 km^2 in size. Machado et al. (1998) and Rossow and Pearl (2007) identified deep convective cloud systems with infrared brightness temperatures less than 245 K. Machado et al. (1998) also stipulated that deep convective cloud systems contain some embedded convective clusters with infrared brightness temperatures less than 218 K. Zuidema (2003) observed organized convective activity over the Bay of Bengal in very cold cloud tops (infrared brightness temperature < 210 K). Other studies used the brightness temperature differences between the upper tropospheric water vapor channel and the window channel to identify penetrating clouds (Soden, 2000; Chung et al., 2008; Young et al., 2012). Soden (2000) identified clouds in the upper troposphere where the differences of the window channel and the upper tropospheric water vapor channel are less than 25 K.

Following the approaches in past studies, we apply these criteria to remove clouds in the upper troposphere: window channel 8 brightness temperature $T_{ch8} \leq 235$ K (cold cloud top), or water vapor channel 12 (at 6.7 μm) brightness temperature $T_{ch12} \leq 210$ K (radiation from a very cold cloud top), or $T_{ch8} - T_{ch12} \leq 25$ K (high channel 12 radiation from cloud-top emission and overlying water vapor emission compared to emission from window channel). The threshold values are adjusted over polar regions to account for the very low temperatures over land and ice surfaces during cold months, for which $T_{ch8} \leq 210 \pm 5$ K (+5 for the northern polar region and −5 for the southern polar

ACPD
12, 33411–33442, 2012

region), $T_{ch12} \leq 200$ K, and $T_{ch8} - T_{ch12} \leq 5$ K. The cloud detection method identifies about 22–25 % of pixels as clouds in the upper troposphere. In a cloud statistics study using HIRS, Wylie et al. (1994) showed that the global total cloud frequency above 400 hPa is 23.9 %. The frequency of upper tropospheric clouds identified in the present work is consistent with the cloud frequencies found in Wylie et al. (1994)'s study and in a subsequent study (Wylie et al., 2005). As a comparison, the cloud-removal process in the previous column-clear-sky version identified about 70 % of pixels as cloudy pixels.

2.2 Comparison with the previous column-clear-sky version

The previous version of the HIRS UTWV data was based on column-clear-sky data (Shi and Bates, 2011). When there was any cloud in the entire column of the atmosphere, the pixel was removed. This included clouds in the mid- and low levels of the atmosphere. Figure 1 exhibits a comparison of the new version with the previous column-clear-sky version for a typical daily observation in a winter month. The data are mapped to $2.5 \times 2.5^{\circ}$ grids. The upper panel displays the new version of UTWV data for 15 January 2011, and the lower panel displays the previous column-clear-sky version for the same day. The areas in black have no data. In the upper panel, though a proportion of pixels are identified as clouds in the upper troposphere and removed, there are usually remaining clear-sky pixels in a grid area, so most grids are filled. For the UTWV brightness temperature observation within the tropics where temperature gradient is small, large brightness temperature values are associated with dry regions where the sensor can "see" to lower atmosphere, while smaller values are associated with moist regions.

Figure 1 shows that for the previous version, large areas of data are removed due to the presence of clouds in any level of the atmosphere. In addition to data associated with convective systems, a lot of these data are associated with low level stratiform clouds. Over a few mid- to high- latitude places, though, there are more missing data in the new version. These places tend to be the areas having very cold temperatures in winter months. For these scenarios the high-level-cloud removal procedure will need

ACPD
12, 33411–33442, 2012

to be improved for future versions. The missing-data areas in the lower panel of Fig. 1 usually correspond to low values of brightness temperatures (indicating high amounts of water vapor) in the upper panel. For the grids that contain data in the lower panel, the brightness temperature values are generally larger than those in the upper panel. When cloudy pixels are removed from a grid area, the remaining column-clear-pixels are usually drier, and thus have higher grid-averaged values of brightness temperatures compared to the same grid in the upper panel. The column-clear-sky version of the dataset is unique in identifying dry areas, but the cloud-removing process essentially removed the UTWV pixels with high water vapor content (pixels with low brightness temperature values). The new version is able to retain the high water vapor content pixels and has a much better spatial coverage of the water vapor field.

Figure 2 compares 33-yr (1979–2011) climatology of the new (top panel) and the previous (middle panel) version. On both maps the locations of maximum and minimum UTWV areas are consistent with each other. Both show low values of brightness temperatures (corresponding to higher humidity) over Indonesia, equatorial South America, and central Africa. High values of brightness temperatures (corresponding to dryer areas) are found over zonal belts along 20° S and 20° N. However the brightness temperature values in the new version are less than those in the previous version. The brightness temperature gradients in the new version are generally larger.

The differences between the new and the previous version are displayed in the bottom panel of Fig. 2. The panel shows that the largest differences (about −5 K) are located over the western equatorial Pacific Ocean and equatorial Indian Ocean, where convective weather systems frequently occur. Large differences of −3 K to −5 K are seen in areas of relatively high cloud frequencies. Most of these areas with large differences overlap with those with total cloud frequencies of more than 80 % in low and mid- latitudes as shown in Wylie et al. (2005). In a grid, the UTWV values of pixels over clouds are generally lower than those of clear-sky pixels due to higher humidity content over clouds. By retaining the pixels over low and middle clouds, the averaged grid values become lower compared to the averaged values of column-clear-sky pixels.

ACPD
12, 33411–33442, 2012

Soden and Lanzante (1996) investigated the impact of the clear-sky sampling restriction upon the HIRS moisture climatology. Their study compared clear-sky and total-sky radiosonde observations and suggested that the clear-sky sampling limitation can introduce a modest dry bias in the satellite derived clear-sky climatology. In a subsequent study, Lanzante and Gahrs (2000) showed that the effects of any such bias are relatively small in the extratropics but may be 5–10 % in the most convectively active regions in the Tropics. The bottom panel of Fig. 2 displays the heterogeneous nature of dry biases. The large dry bias resulted from clear-sky sampling is located over the equatorial western Pacific Ocean with extension to the Eastern Indian Ocean. The dry bias is much smaller over the southern low-latitude eastern Pacific Ocean and the southern low-latitude Atlantic Ocean. In a study that used microwave sounder measurements to examine column-clear-sky sampling issues, John et al. (2011) illustrated bias values in terms of relative humidity for January and July 2008. Many of the areas with differences of −3 K to −5 K in Fig. 2 of the present study are in the areas with column-clear-sky relative humidity bias values of −5 % to −15 % in Fig. 7 of John et al. (2011).

There are several areas where differences between the new and the previous version are close to zero. Over the low and mid- latitudes these small difference areas are located in the eastern South Pacific between the equator and 30° S, the South Atlantic between the equator and 30° S, and the northern Africa and Saudi Arabia. These small difference areas mostly correspond to places with less cloud coverage. Where cloud is rare, the difference between the two UTWV versions is minimal.

2.3 Monthly climatology

Using 33 yr of data from 1979 to 2011, we derived the climatological mean of each month (Fig. 3). The basic patterns in the tropics are similar to those in Wu et al. (1993), who displayed 1981–1988 UTWV monthly climatology from 45° N to 45° S. Figure 3 shows that in January, there is a long dry belt in the northern tropics, strongest over the tropical Pacific. The driest regions are usually in the descending branch of the

ACPD
12, 33411–33442, 2012

general circulation such as the Hadley Cell. An UTWV image is often better at locating the descending branch of the general circulation than are fields of cloud or outgoing longwave radiation because neither of those fields can tell if one cloud-free region is dryer than another, but the water vapor field can. In January, moist regions are found south of the equator. The organized moist belt is usually associated with the Intertropical Convergence Zone (ITCZ). In July, the moist regions are north of the equator, while the driest belt is in the southern tropics. The brightness temperature gradient is smallest in April, indicating weak general circulations.

3 Comparison of HIRS and microwave sounder measurements

3.1 Microwave sounder data

The Advanced Microwave Sounder Unit-B (AMSU-B) instruments have been onboard NOAA satellites NOAA-15 to NOAA-17. A similar instrument, Microwave Humidity Sounder (MHS), has been on board the satellites in the Initial Joint Polar-Orbiting Operational Satellite System (IJPS) series. Among several channels on the microwave sounders, one channel is in 183.31+/−1.00 GHz for making measurements of upper tropospheric water vapor. Microwave observations are affected by precipitating ice clouds, therefore ice cloud pixels are removed using a method developed by Buehler et al. (2007). Data from microwave sounders on NOAA-17 and METOP-A (one of the satellites in the IJPS series) are then combined to obtain daily gridded files of brightness temperatures on a $2.5 \times 2.5^{\circ}$ resolution. The comparison is done only for January and July 2008, similar to the analyses of John et al. (2011).

3.2 Comparison results

Figure 4 displays HIRS and microwave UTWV brightness temperatures and their differences for January and July 2008. Bottom panels show the differences (microwave minus HIRS) as functions of microwave brightness temperatures. Red symbols show

ACPD
12, 33411–33442, 2012

mean differences and their standard deviations for 5 K brightness temperature bins. John et al. (2011) compared almost-all-sky and column-clear-sky AMSU-B upper tropospheric humidity, and found that there is considerable bias in the column-clear-sky data set compared to almost-all-sky microwave measurements due to under-sampling of humid cases in the presence of clouds. They also showed that the clear-sky bias is significantly correlated with upper tropospheric humidity. In the present study we do a similar analysis to see how the new version of HIRS data compares with microwave measurements and whether the differences have a dependence on the humidity values.

Higher HIRS brightness temperatures are measured in the dry subsidence regions and lower brightness temperatures are measured over convectively active, humid ITCZ and monsoon regions (Fig. 4a and b). Microwave brightness temperatures displayed in panels c and d show similar patterns as those in panels a and b, but are about 7–10 K higher compared to HIRS brightness temperatures, owing to differences in water vapor emissivity at infrared and microwave frequencies. The microwave measurements are sensitive to a slightly lower layer in the upper troposphere compared to HIRS measurements, which also contributes to the differences.

The difference between the brightness temperatures should be larger for dry regions and smaller for humid regions because in a drier atmosphere the microwave channel requires a longer path length to get saturated compared to that in a humid atmosphere, so it samples a lower level of the atmosphere. Panels e and f show the distribution of brightness temperature differences and panels g and h show the brightness temperature differences as a function of microwave brightness temperatures. On average microwave brightness temperatures are 9 K higher than HIRS brightness temperatures for very dry cases (> 265 K). As the brightness temperatures become lower, the differences decrease. At about 250 K the differences start to increase slightly with decreasing brightness temperatures for very wet cases. This differs from the clear-sky bias shown in John et al. (2011). The increased differences for brightness temperatures below 250 K indicate the possibility of a few cloudy pixels being included in the

ACPD
12, 33411–33442, 2012

new HIRS data set. These cloudy pixels may come from thin cirrus clouds that are difficult to detect or from clouds with tops in the lower portion of the upper troposphere.

4 A survey of UTWV correlations with climate indices

The analysis of column-clear-sky UTWV by Shi and Bates (2011) showed that distributions of UTWV are closely related to several climate indices, including the Pacific Decadal Oscillation (PDO) index, the Pacific and North America (PNA) index, and the East Central Tropical Pacific Sea Surface Temperature (Nino3.4) index. As an update, the one-point (pairwise) correlation maps between channel 12 brightness temperatures and these climate indices are re-computed using the new version of HIRS UTWV. In the present study we also extend the examination to several additional, widely used climate indices, including the North Atlantic Oscillation (NAO), Artic Oscillation (AO), and Antarctic Oscillation (AAO) indices to provide a survey of the relationship of UTWV with a wider range of major climate indices. The selected climate indices cover different geographic regions from the tropics to the poles, and their phases range from weeks to multi-decades. The mean distribution of water vapor in the upper troposphere is a result of large-scale circulations. The correlations can show how closely the UTWV distribution relates to the atmospheric variables used in tracking climate indices. The analysis also detects teleconnection patterns of UTWV with climate indices in various regions of the world.

4.1 Correlation with Niño 3.4 index

The Niño 3.4 index is based on the anomalies of sea surface temperature (SST) of the region 5° N–5° S and 120–170° W. It is often used to define El Niño – Southern Oscillation (ENSO) events (Trenberth, 1997). To objectively locate areas that have large association with ENSO, we computed correlations between the time series of UTWV at each grid point and the time series of Niño 3.4 SST anomaly (Fig. 5). The top panel

ACPD
12, 33411–33442, 2012

displays the correlation map taking each of the months into consideration (labelled as "Year-round"). The middle and bottom panels display correlation maps for December, January, and February (DJF) and for June, July, and August (JJA), respectively. As lower values of UTWV brightness temperatures generally represent higher water vapor contents, negative correlations (blue colors) in the figure reflect positive correlations between higher water vapor and Niño 3.4 index.

The top panel shows that the highest absolute correlation (−0.6) between UTWV brightness temperatures and Niño 3.4 anomalies is over the central equatorial Pacific. The highest correlation of the opposite sign (0.6) is centered over the western Pacific near Indonesia. Positive correlation areas are also found in the subtropics, one at 20–30° N and another at 20–30° S over the Pacific. These areas with positive correlations correspond to descending branches of the atmospheric circulations. When Niño 3.4 SST increases, the atmospheric circulation transports more moisture into the upper troposphere over the central and eastern equatorial Pacific, while the subsidence dries the upper troposphere over both the northern and southern subtropical Pacific. The increase of SST in the eastern Pacific can affect regions outside of the tropics by altering prevailing wind patterns around the globe. For example, negative correlations (positive correlations between water vapor and Niño 3.4 SST) are found over the subtropical South Indian Ocean and eastern South Pacific Ocean. The DJF correlation pattern (middle panel) is similar to the year-round pattern, but with higher correlations in both negative and positive regions, confirming that the ENSO events are more active during the boreal winter season. During JJA (lower panel) the correlation pattern differs significantly from that in DJF. Though there is still a high negative correlation belt along the central equatorial Pacific, the high positive correlation area over the northern subtropical Pacific is largely replaced by negative correlations, indicating a different location of the descending branch of general circulation in JJA.

ACPD
12, 33411–33442, 2012

4.2 Correlation with PDO index

The PDO index is tracked from observed Pacific Ocean SST and sea level pressure patterns (Mantua et al., 1997). The signature of PDO is most significant in the North Pacific and North America, with secondary signatures in the tropics (Mantua and Hare, 2002). Minobe (1999) found that 20th century PDO fluctuations were most energetic around bidecadal and half-century time-scales. PDO phases are much longer than ENSO events which typically last for 6 to 18 months. However, there is a strong linkage between PDO and ENSO events. For example, Newman et al. (2003) found that both interannual and decadal timescales of PDO can be well modeled as the sum of direct forcing by ENSO.

The correlations between channel 12 brightness temperatures and the PDO index are shown in Fig. 6. Negative correlations with brightness temperature reflect positive correlations between water vapor and the PDO index. The middle panel of Fig. 6 shows that in DJF relatively large negative correlations are found in mid-latitudes of the Pacific Ocean and in the eastern-central equatorial Pacific. There is a positive correlation area in the eastern Pacific near 20° N. In JJA, the correlation pattern in the northern Pacific Ocean is less distinct compared to DJF. Taking 12 months into consideration, there is a negative correlation belt extending from the mid-latitude Pacific Ocean, across the Asian continent, and into Europe. Subsidence along 20–30° N over the Pacific reduces water vapor and enhances positive correlations with brightness temperature.

4.3 Correlation with PNA index

The PNA pattern is one of the low-frequency variabilities in the northern extratropics. Wallace and Gutzler (1981) first identified the correlated mid- to upper-tropospheric geopotential heights over the North Pacific and North America. The positive phase of the PNA is characterized by a region of above-average geopotential heights at 500 hPa and 700 hPa in northern Canada and the northweastern United States and an area around Hawaii. In the meantime below-average geopotential heights are centered in

ACPD
12, 33411–33442, 2012

mid- to high latitudes over the North Pacific and in the southeastern United States. Calculation of the PNA index was described in detail by Barnston and Livezey (1987), and the sensitivity of the index and the pattern to analysis technique were also studied by van den Dool et al. (2000) and Chen and Van den Dool (2003). The PNA pattern is present on time scales from weeks to years (Blackmon et al., 1984). Studies found that the PNA index is closely related to regional climate in various parts of the world such as temperature and precipitation of the United States (Leathers et al., 1991), Indian summer monsoon rainfall (Peings et al., 2009), and sea ice over the western Arctic (L'Heureux et al., 2008).

Figure 7 displays the correlations of HIRS channel 12 brightness temperatures with the PNA index. The lower left panel of Fig. 7 shows that during boreal winter (DJF) there are high correlations of UTWV with the PNA index. The PNA is associated with a wave train that originates in the subtropical Pacific, extends northeastward to North America, and then reflects southeastward to the tropical Atlantic. Evidence for this wave train can be seen in the alternating positive and negative correlations with UTWV. Particularly notable is the broad area of positive correlations near Hawaii. The positive PNA is associated with an enhanced subtropical ridge in this region, and the positive correlations are consistent with the associated drying. Schreck et al. (2012) found a similar relationship between UTWV and the subtropical ridge that was associated with the Madden-Julian Oscillation. The PNA is a winter pattern so during boreal summer (JJA) the correlations are generally small. The year-round pattern (top panel of Fig. 7) is similar to but weaker than that for DJF. Compared to a typical positive phase of PNA pattern in which there is a region of below-average geopotential heights over the southeastern United States, the UTWV year-round correlation map shows negative correlations in lower latitudes (around Cuba) and extends more significantly to the east. The southward-displaced negative correlations are likely the result of higher water vapor content in the tropics.

ACPD
12, 33411–33442, 2012

4.4 Correlation with NAO index

Another low-frequency pattern that reflects large-scale changes in the atmospheric wave and jet stream patterns over North America, Europe, and North Africa is tracked as the NAO index. The NAO pattern was also identified by Wallace and Gutzler (1981). The positive phase of NAO is characterized by above-average geopotential heights over the subtropical-midlatitude Atlantic Ocean and western Europe. There is an area of associated below-average geopotential heights around Greenland and Iceland. In summer the NAO has a smaller geographical scale than in winter, and low pressure over Greenland is associated with high pressure from the United Kingdom to Scandinavia (Folland et al., 2009). Many studies showed profound influences of NAO on various regional climates, such as the North Atlantic cloud cover and marine response to NAO (Previdi and Veron, 2007; Patara et al., 2011), teleconnection between NAO and climate downstream of the Tibetan Plateau (Li et al., 2008), the influence of NAO on European precipitation (Vicente-Serrano and López-Moreno, 2008; Folland et al., 2009), the influence of NAO on air pollution transport (Christoudias et al., 2012), and the relationship of Great Lakes ice cover variability to NAO (Bai et al., 2012).

Figure 8 displays the correlation map between HIRS channel 12 brightness temperatures and NAO. In winter (lower left panel) the correlation pattern is in good agreement with the positive phase of NAO. High positive correlations (dry air) are found over Mediterranean and Europe. Other positive correlation areas are located over the United States, eastern Russia, and an area stretching from Arabian Sea and southern India to the northern Indian Ocean. There is a center with large negative correlations over Greenland. Another negative correlation area around 10° N of the eastern Atlantic is also prominant. During summer months (lower right panel) the limited area of modest possitive correlations over Europe is consistent with the high pressure region described by Folland et al. (2009). The year-round correlation map also resembles the positive phase of the winter NAO, but is weaker.

ACPD
12, 33411–33442, 2012

4.5 Correlations with AA and AAO indices

With observations from polar-orbiting satellites, HIRS data have a complete areal coverage of the polar regions on a daily basis. This makes it possible to examine the correlations of HIRS channel 12 brightness temperatures with two polar climate indices, the AO and AAO. The patterns of AO and AAO are defined as the first leading mode from the emperical orthogonal function analysis of monthly mean height anomalies at 1000 hPa in the Northern Hemisphere for AO and at 700 hPa in the Southern Hemisphere for AAO. In the positive phase of AO, there is a positive anomaly region over the eastern North Atlantic and western Europe between 40° and 50° N, and another positive region over the central North Pacific at 50° N. Negative anomalies are found around the north pole. In the positive phase of AAO, there is a belt of positive anomalies in the southern Indian Ocean between 40° and 50° S and there is another positive anomaly region in the southern Pacific near southern New Zealand. Negative anomalies are centered over Antarctica.

The AO and AAO have profound influences on environmental variables in high latitude regions. For example, Yu et al. (2012) used both surface observational data and global models to show that among several climate indices including the AAO, the Pacific-South American teleconnection and ENSO, the most important contribution to the trends of Antarctic sea level pressure and surface temperature comes from AAO. Numerous studies showed that AO and AAO also have far-reaching influences beyond polar regions. Lim and Schubert (2011) revealed that both winter mean temperature anomalies and the number of days of extreme cold in the southeast United States are closely linked to variations in AO especially in the recent past (1981–2008). Choi et al. (2012) showed that the frequency of summer tropical cyclones in Japan, Korea, and Taiwan in the middle latitudes of East Asia, has a positive correlation with AO occurring during the preceding spring, while summer tropical cyclone frequency in the Philippines, located in the low latitudes, has a negative correlation with the AO of the preceding spring. Park et al. (2011) studied changes in the characteristics of cold

ACPD
12, 33411–33442, 2012

surges over East Asia associated with the Arctic Oscillation (AO) and found that the blocking type of cold surge tends to occur during negative AO periods. Since the AO and AAO have the largest variability during the cold sesaons, the loading patterns primarily capture characteristics of the cold season patterns. However, Rigor et al. (2002) found that the memory of the wintertime AO has its signals through most of the subsequent year. Spring and autumn surface air temperature and summertime sea ice concentration are all strongly correlated with the AO index for the previous winter. It was hypothesized that these delayed responses reflect the dynamical influence of the AO on the thickness of the wintertime sea ice, whose persistent "footprint" is reflected in the heat fluxes during the subsequent spring, in the extent of open water during the subsequent summer, and the heat liberated in the freezing of the open water during the subsequent autumn.

Figures 9 and 10 display the correlations of HIRS channel 12 brightness temperatures with AO and AAO, respectively. Figure 9 shows that the highest positive correlation with the AO is found in DJF over Europe. The year-round pattern is similar to the DJF pattern, but weaker. Comparing to the positive AO 1000 hPa geopotential pattern, the most significant positive correlation region over eastern North Atlantic and Europe in the DJF and year-round maps is slightly further east. Unlike the positive phase of AO where there is a single positive geopotential anomaly area over the central North Pacific in the AO EOF pattern of 1000 hPa height anomalies, in both the DJF and the year-round correlation maps there are two possitive correlation centers, one over northeast Asia and another over the northwestern United States. The differences compared to the 1000 hPa height anomaly AO pattern may be due to drier air over land surfaces reflected by higher brightness temperatures compared to ocean surfaces. In Figure 10, the JJA map and year-round map for southern high latitudes closely resemble the positive phase of AAO. On the JJA map, in addition to the positive anomaly centers of the AAO positive phase, there are large positive correlations over the Southeast Pacific, southern Africa, the midlatitude South Atlantic, and near the equator at 150° E.

ACPD
12, 33411–33442, 2012

These high positive correlation features show strong hemisphere-wide teleconnections of AAO.

5 Summary

A new version of the HIRS UTWV dataset is developed using intersatellite calibrated all-sky data. In this dataset the only removed pixels are those containing clouds in the upper troposphere. Pixels with clouds in the mid- and lower troposphere remain in the dataset because they do not affect the processing of water vapor in the upper troposphere. Compared to the previous version of column-clear-sky HIRS UTWV dataset, the new version is able to retain pixels with high water vapor content and provide a much better spatial coverage on a daily basis and better represent the water vapor field in the upper troposphere.

The observations from HIRS and from microwave sounder measurements show very similar patterns, though HIRS measurements are about 7–10 K colder than those from microwave sounders. The differences are larger for dry regions over which the microwave channel requires a longer path length to become saturated so it samples a lower atmospheric level. The differences for cold brightness temperatures are slightly larger due to possible inclusions of cloudy pixels.

Correlations of UTWV with several major climate indices that represent climate variabilities ranging from the tropics to the poles are examined. The correlation patterns with Niño 3.4, PDO, and PNA indices are very similar to the results derived from the previous version of column-clear-sky UTWV shown in Shi and Bates (2011), confirming that either the new version or column-clear-sky version is able to capture climate variabilities in terms of correlations with major climate indices. In the present study, correlations of UTWV with NAO, AO, and AAO indices are also calculated. The correlation patterns in the cold seasons generally match the positive phases of these high-latitude climate indices, though the locations of highest correlations may differ slightly. The distribution of water vapor in the upper troposphere is a result of atmospheric general

ACPD
12, 33411–33442, 2012

circulations. The correlation analysis shows the potential of using UTWV in monitoring long-term changes in large-scale atmospheric circulation and in locating teleconnections of regional systems with major global climate systems.

As the new version of UTWV dataset is able to provide much better daily spatial coverage, it can be used to track the movement of weather systems globally on daily basis. For example, the use of HIRS UTWV to track tropical waves is explored in Schreck et al. (2012). HIRS UTWV clearly identifies the variance associated with the Madden–Julian oscillation, equatorial Rossby waves, and Kelvin waves, as well as the subsidence drying that occurs poleward of the MJO's convection in the subtropics. With daily global observation, the UTWV dataset adds to the suite of observational measurements for monitoring weather and climate systems.

Acknowledgements. The authors thank Darren Jackson of Cooperative Institute for Research in Environmental Sciences, University of Colorado at Boulder for providing all-sky HIRS/2 data. The Niño 3.4, PDO, PDA, NAO, AA, and AAO indices are obtained from NOAA Climate Prediction Center. Carl Schreck received support for this study from NOAA NCDC's Climate Data Record Program. Viju John was supported by the Joint DECC/Defra Met Office Hadley Centre Climate Programme (GA01101), the UK JWCRP, and EUMETSAT CMSAF. We thank David Parker of UK Met Office for valuable comments.

References

Bai, X., Wang, J., Sellinger, C., Clites, A., and Assel, R.: Interannual variability of Great Lakes ice cover and its relationship to NAO and ENSO, J. Geophys. Res., 117, C03002, doi:10.1029/2010jc006932, 2012.

Barnston, A. G. and Livezey, R. E.: Classification, Seasonality and Persistence of Low-Frequency Atmospheric Circulation Patterns, Mon. Weather Rev., 115, 1083–1126, doi:10.1175/1520-0493(1987)115¡1083:csapol¿2.0.co;2, 1987.

Bates, J. J. and Jackson, D. L.: Trends in upper-tropospheric humidity, Geophys. Res. Lett., 28, 1695–1698, 2001.

ACPD

12, 33411–33442, 2012

Bates, J. J., Wu, X., and Jackson, D. L.: Interannual variability of upper-troposphere water vapor band brightness temperature, J. Climate, 9, 427–438, 1996.
Bates, J. J., Jackson, D. L., Breon, F. M., and Bergen, Z. D.: Variability of tropical upper tropospheric humidity 1979–1998, J. Geophys. Res.-Atmos., 106, 32271–32281, 2001.
Blackmon, M. L., Lee, Y. H., and Wallace, J. M.: Horizontal Structure of 500 mb Height Fluctuations with Long, Intermediate and Short Time Scales, J. Atmos. Sci., 41, 961–980, doi:10.1175/1520-0469(1984)041¡0961:hsomhf¿2.0.co;2, 1984.
Buehler, S. A., Kuvatov, M., Sreerekha, T. R., John, V. O., Rydberg, B., Eriksson, P., and Notholt, J.: A cloud filtering method for microwave upper tropospheric humidity measurements, Atmos. Chem. Phys., 7, 5531–5542, doi:10.5194/acp-7-5531-2007, 2007.
Chen, W. Y. and Van den Dool, H.: Sensitivity of Teleconnection Patterns to the Sign of Their Primary Action Center, Mon. Weather Rev., 131, 2885–2899, doi:10.1175/1520-0493(2003)131¡2885:sotptt¿2.0.co;2, 2003.
Choi, K. S., Wu, C. C., and Byun, H. R.: Possible connection between summer tropical cyclone frequency and spring Arctic Oscillation over East Asia, Clim. Dynam., 38, 2613–2629, doi:10.1007/s00382-011-1088-z, 2012.
Christoudias, T., Pozzer, A., and Lelieveld, J.: Influence of the North Atlantic Oscillation on air pollution transport, Atmos. Chem. Phys., 12, 869–877, doi:10.5194/acp-12-869-2012, 2012.
Chung, E. S., Sohn, B. J., and Schmetz, J.: CloudSat shedding new light on high-reaching tropical deep convection observed with Meteosat, Geophys. Res. Lett., 35, L02814, doi:10.1029/2007gl032516, 2008.
Folland, C. K., Knight, J., Linderholm, H. W., Fereday, D., Ineson, S., and Hurrell, J. W.: The Summer North Atlantic Oscillation: Past, Present, and Future, J. Climate, 22, 1082–1103, doi:10.1175/2008jcli2459.1, 2009.
Geer, A. J., Harries, J. E., and Brindley, H. E.: Spatial patterns of climate variability in upper-tropospheric water vapor radiances from satellite data and climate model simulations, J. Climate, 12, 1940–1955, 1999.
Iacono, M. J., Delamere, J. S., Mlawer, E. J., and Clough, S. A.: Evaluation of upper tropospheric water vapor in the NCAR Community Climate Model (CCM3) using modeled and observed HIRS radiances, J. Geophys. Res.-Atmos., 108, 4037, doi:10.1029/2002jd002539, 2003.
John, V. O., Holl, G., Allan, R. P., Buehler, S. A., Parker, D. E., and Soden, B. J.: Clear-sky biases in satellite infrared estimates of upper tropospheric humidity and its trends, J. Geophys. Res.-Atmos., 116, D14108, doi:10.1029/2010jd015355, 2011.

ACPD
12, 33411–33442, 2012

L'Heureux, M. L., Kumar, A., Bell, G. D., Halpert, M. S., and Higgins, R. W.: Role of the Pacific-North American (PNA) pattern in the 2007 Arctic sea ice decline, Geophys. Res. Lett., 35, L20701, doi:10.1029/2008gl035205, 2008.

Lanzante, J. R. and Gahrs, G. E.: The "Clear-Sky Bias" of TOVS Upper-Tropospheric Humidity, J. Climate, 13, 4034–4041, doi:10.1175/1520-0442(2000)013¡4034:tcsbot¿2.0.co;2, 2000.

Leathers, D. J., Yarnal, B., and Palecki, M. A.: The Pacific/North American Teleconnection Pattern and United States Climate, Part I: Regional Temperature and Precipitation Associations, J. Climate, 4, 517–528, doi:10.1175/1520-0442(1991)004¡0517:tpatpa¿2.0.co;2, 1991.

Li, J., Yu, R., and Zhou, T.: Teleconnection between NAO and Climate Downstream of the Tibetan Plateau, J. Climate, 21, 4680–4690, doi:10.1175/2008jcli2053.1, 2008.

Lim, Y. K. and Schubert, S. D.: The impact of ENSO and the Arctic Oscillation on winter temperature extremes in the southeast United States, Geophys. Res. Lett., 38, L15706, doi:10.1029/2011gl048283, 2011.

Machado, L. A. T., Rossow, W. B., Guedes, R. L., and Walker, A. W.: Life cycle variations of mesoscale convective systems over the Americas, Mon. Weather Rev., 126, 1630–1654, 1998.

Mantua, N. J., Hare, S. R., Zhang, Y., Wallace, J. M., and Francis, R. C.: A Pacific interdecadal climate oscillation with impacts on salmon production, B. Am. Meteorol. Soc., 78, 1069–1079, 1997.

Mantua, N. J. and Hare, S. R.: The Pacific decadal oscillation, J. Oceanogr., 58, 35–44, 2002.

Mapes, B. E. and Houze, R. A.: Cloud Clusters and Superclusters over the Oceanic Warm Pool, Mon. Weather Rev., 121, 1398–1415, 1993.

McCarthy, M. P. and Toumi, R.: Observed interannual variability of tropical troposphere relative humidity, J. Climate, 17, 3181–3191, 2004.

Newman, M., Compo, G. P., and Alexander, M. A.: ENSO-Forced Variability of the Pacific Decadal Oscillation, J. Climate, 16, 3853–3857, doi:10.1175/1520-0442(2003)016¡3853:evotpd¿2.0.co;2, 2003.

Park, T. W., Ho, C. H., and Yang, S.: Relationship between the Arctic Oscillation and Cold Surges over East Asia, J. Climate, 24, 68–83, doi:10.1175/2010jcli3529.1, 2011.

Patara, L., Visbeck, M., Masina, S., Krahmann, G., and Vichi, M.: Marine biogeochemical responses to the North Atlantic Oscillation in a coupled climate model, J. Geophys. Res., 116, C07023, doi:10.1029/2010jc006785, 2011.

ACPD
12, 33411–33442, 2012

Peings, Y., Douville, H., and Terray, P.: Extended winter Pacific North America oscillation as a precursor of the Indian summer monsoon rainfall, Geophys. Res. Lett., 36, L11710, doi:10.1029/2009gl038453, 2009.
Previdi, M. and Veron, D. E.: North Atlantic cloud cover response to the North Atlantic oscillation and relationship to surface temperature changes, J. Geophys. Res., 112, D07104, doi:10.1029/2006jd007516, 2007.
Rigor, I. G., Wallace, J. M., and Colony, R. L.: Response of Sea Ice to the Arctic Oscillation, J. Climate, 15, 2648–2663, doi:10.1175/1520-0442(2002)015¡2648:rositt¿2.0.co;2, 2002.
Rossow, W. B. and Pearl, C.: 22-Year survey of tropical convection penetrating into the lower stratosphere, Geophys. Res. Lett., 34, L04803, doi:10.1029/2006gl028635, 2007.
Schreck, C. J., Shi, L., Kossin, J. P., and Bates, J. J.: Identifying the MJO, Equatorial Waves, and Their Impacts Using 32 Years of HIRS Upper Tropospheric Water Vapor, J. Climate, in press, 2012.
Shi, L. and Bates, J. J.: Three decades of intersatellite-calibrated High-Resolution Infrared Radiation Sounder upper tropospheric water vapor, J. Geophys. Res.-Atmos., 116, D04108, doi:10.1029/2010jd014847, 2011.
Shi, L., Bates, J. J., and Cao, C.: Scene Radiance–Dependent Intersatellite Biases of HIRS Longwave Channels, J. Atmos. Ocean Tech., 25, 2219–2229, doi:10.1175/2008jtecha1058.1, 2008.
Soden, B. J.: The diurnal cycle of convection, clouds, and water vapor in the tropical upper troposphere, Geophys. Res. Lett., 27, 2173–2176, 2000.
Soden, B. J. and Lanzante, J. R.: An assessment of satellite and radiosonde climatologies of upper-tropospheric water vapor, J. Climate, 9, 1235–1250, 1996.
Soden, B. J., Jackson, D. L., Ramaswamy, V., Schwarzkopf, M. D., and Huang, X. L.: The radiative signature of upper tropospheric moistening, Science, 310, 841–844, doi:10.1126/science.1115602, 2005.
Sohn, B. J. and Park, S.-C.: Strengthened tropical circulations in past three decades inferred from water vapor transport, J. Geophys. Res., 115, D15112, doi:10.1029/2009jd013713, 2010.
Trenberth, K. E.: The definition of El Niño, B. Am. Meteorol. Soc., 78, 2771–2777, 1997.
van den Dool, H. M., Saha, S., and Johansson, Å.: Empirical Orthogonal Teleconnections, J. Climate, 13, 1421–1435, doi:10.1175/1520-0442(2000)013¡1421:eot¿2.0.co;2, 2000.

ACPD
12, 33411–33442, 2012

Vicente-Serrano, S. M. and López-Moreno, J. I.: Nonstationary influence of the North Atlantic Oscillation on European precipitation, J. Geophys. Res., 113, D20120, doi:10.1029/2008jd010382, 2008.
Wallace, J. M. and Gutzler, D. S.: Teleconnections in the Geopotential Height Field during the Northern Hemisphere Winter, Mon. Weather Rev., 109, 784–812, doi:10.1175/1520-0493(1981)109¡0784:titghf¿2.0.co;2, 1981.
Wu, X. Q., Bates, J. J., and Khalsa, S. J. S.: A Climatology of the Water-Vapor Band Brightness Temperatures from Noaa Operational Satellites, J. Climate, 6, 1282–1300, 1993.
Wylie, D., Jackson, D. L., Menzel, W. P., and Bates, J. J.: Trends in global cloud cover in two decades of HIRS observations, J. Climate, 18, 3021–3031, 2005.
Wylie, D., Eloranta, E., Spinhirne, J. D., and Palm, S. P.: Comparison of cloud cover statistics from the GLAS lidar with HIRS, J. Climate, 20, 4968–4981, doi:10.1175/Jcli4269.1, 2007.
Wylie, D. P., Menzel, W. P., Woolf, H. M., and Strabala, K. I.: 4 Years of Global Cirrus Cloud Statistics Using Hirs, J. Climate, 7, 1972–1986, 1994.
Young, A. H., Bates, J. J., and Curry, J. A.: Complementary use of passive and active remote sensing for detection of penetrating convection from CloudSat, CALIPSO, and Aqua MODIS, J. Geophys. Res., 117, D13205, doi:10.1029/2011jd016749, 2012.
Yu, L. J., Zhang, Z. H., Zhou, M. Y., Zhong, S., Lenschow, D., Hsu, H. M., Wu, H. D., and Sun, B.: Influence of the Antarctic Oscillation, the Pacific-South American modes and the El Niño-Southern Oscillation on the Antarctic surface temperature and pressure variations, Antarct. Sci., 24, 59–76, doi:10.1017/S095410201100054x, 2012.
Zuidema, P.: Convective clouds over the Bay of Bengal, Mon. Weather Rev., 131, 780–798, 2003.

ACPD
12, 33411–33442, 2012

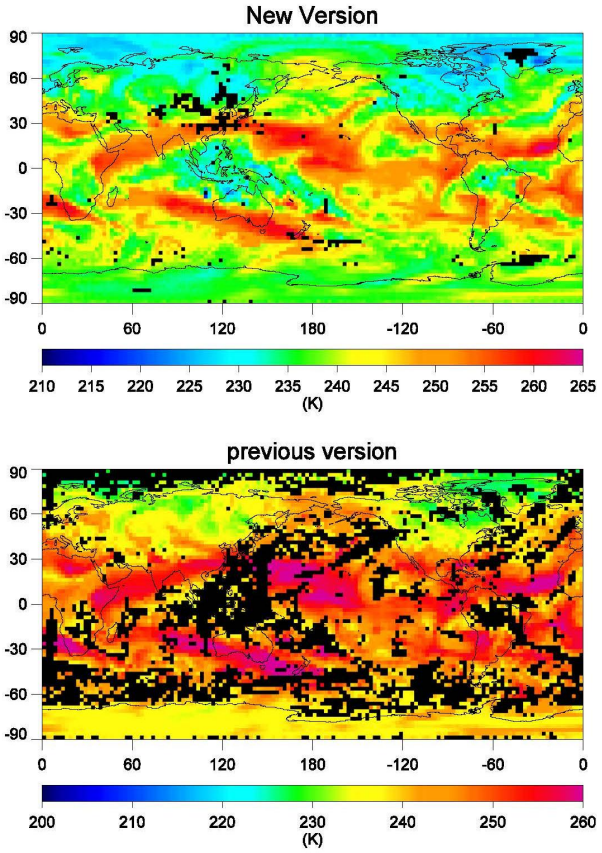

Fig. 1. Comparison of one-day's spatial coverage between the new version and the previous column-clear-sky version of Shi and Bates (2011). The example is taken from METOP-A observation on 15 January 2011.

ACPD
12, 33411–33442, 2012

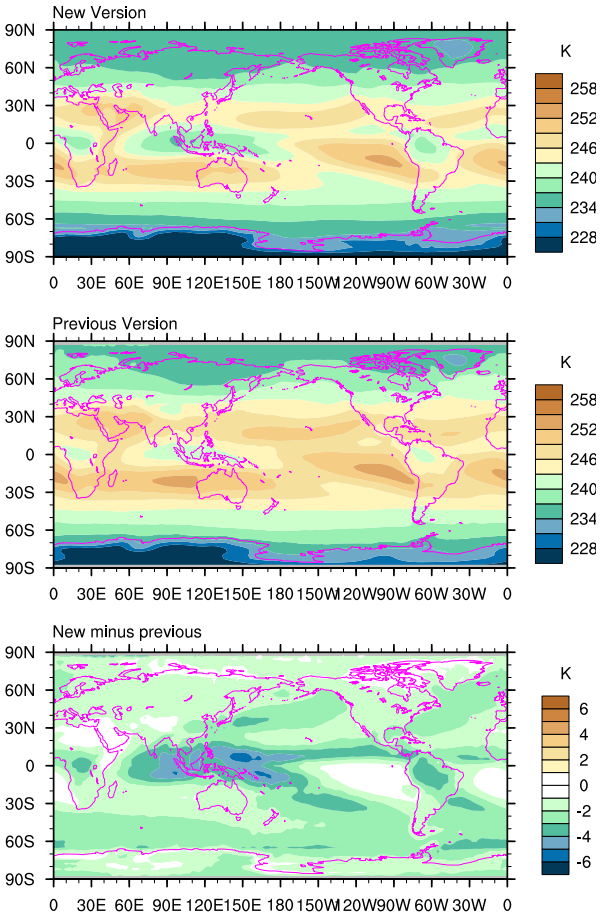

Fig. 2. The 33-yr (1979–2011) HIRS UTWV climatology maps for the new version (top panel) and the previous column-clear-sky version of Shi and Bates (2011) (middle panel). The bottom panel shows the difference between the two versions.

ACPD
12, 33411–33442, 2012

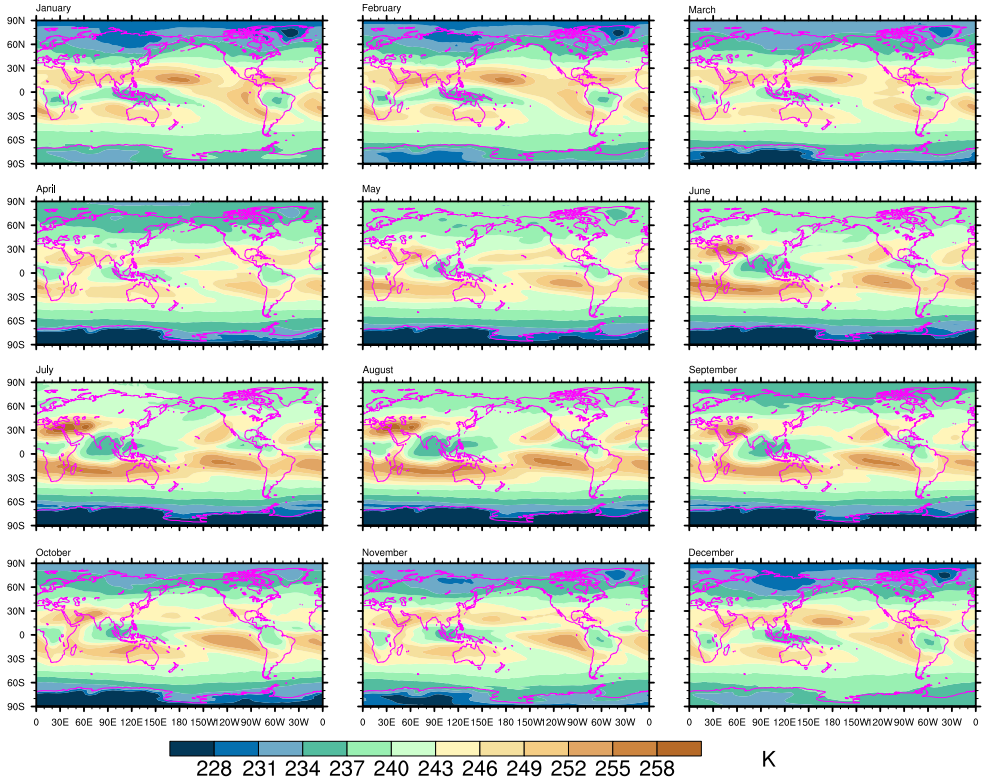

Fig. 3. Monthly climatology of HIRS UTWV based on data from 1979–2011.

ACPD
12, 33411–33442, 2012

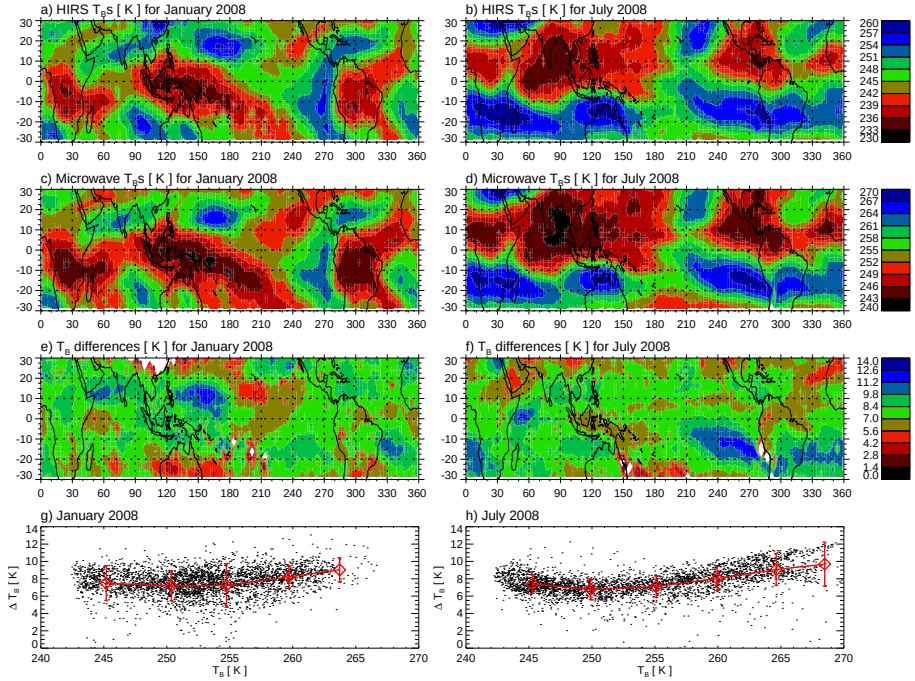

Fig. 4. HIRS and microwave UTWV brightness temperatures (T_Bs) and their differences for (left) January and for (right) July 2008. Bottom panels show the differences (microwave minus HIRS) as function of microwave T_Bs. Red symbols show mean differences and their standard deviations for 5 K Tb bins.

ACPD
12, 33411–33442, 2012

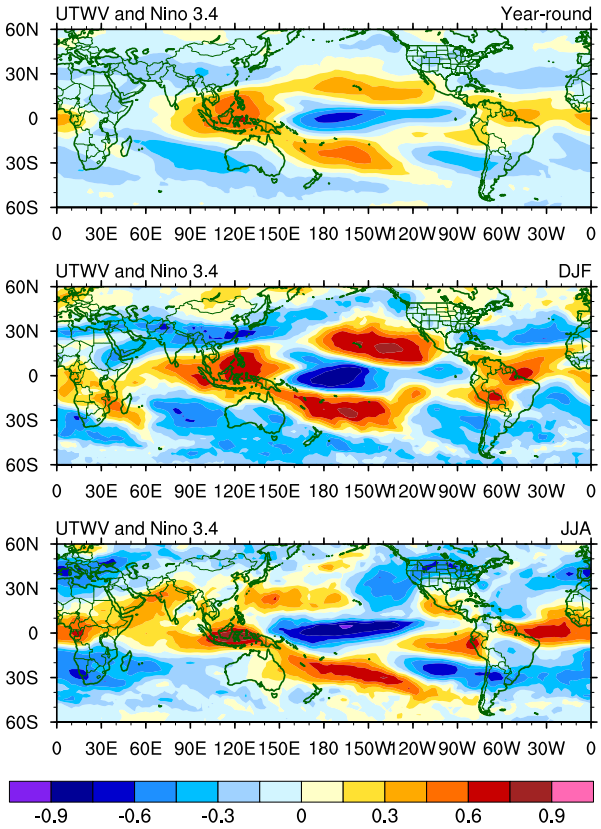

Fig. 5. Correlations between UTWV brightness temperature and Niño 3.4 index for year-round, DJF, and JJA.

ACPD
12, 33411–33442, 2012

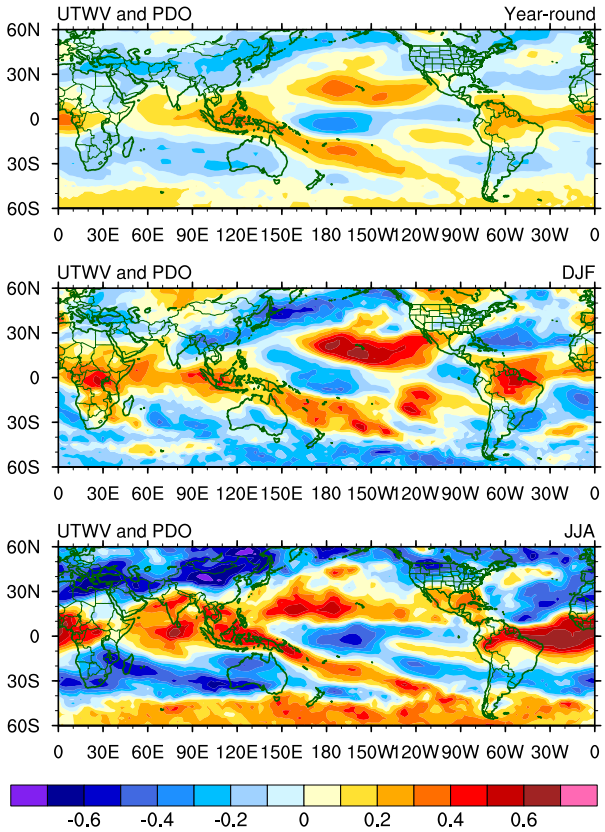

Fig. 6. Correlations between UTWV brightness temperature and PDO index for year-round, DJF, and JJA.

ACPD
12, 33411–33442, 2012

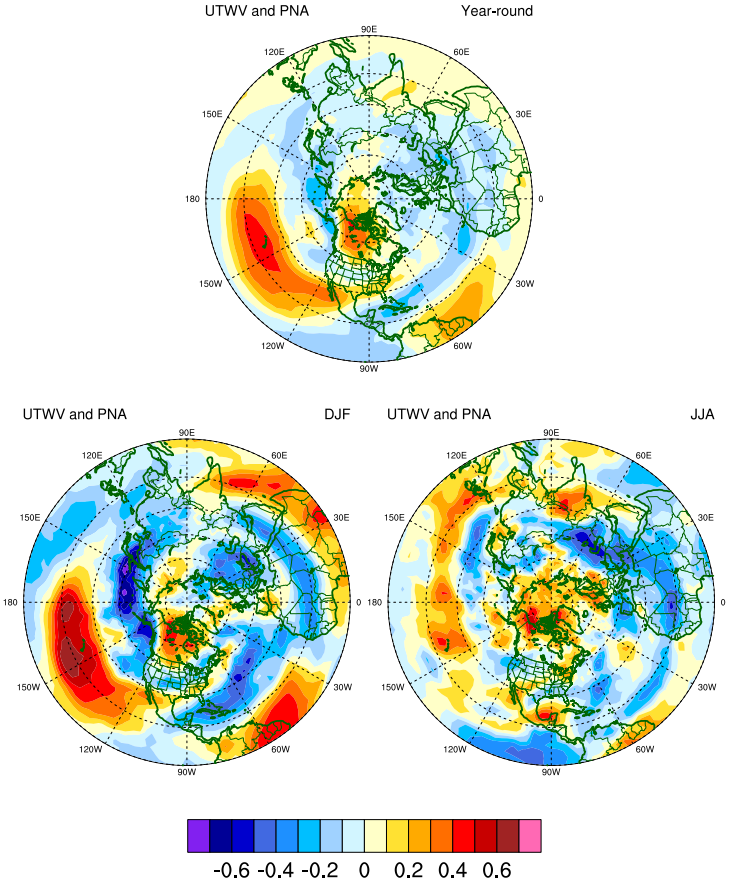

Fig. 7. Correlations between UTWV brightness temperature and PNA index for year-round, DJF, and JJA.

ACPD
12, 33411–33442, 2012

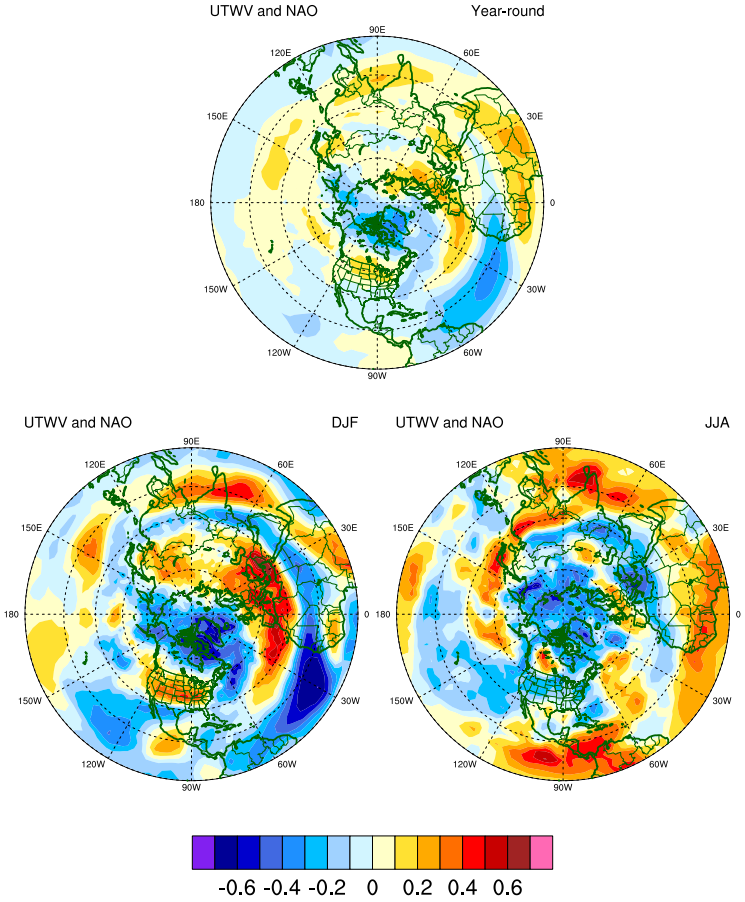

Fig. 8. Correlations between UTWV brightness temperature and NAO index for year-round, DJF, and JJA.

ACPD
12, 33411–33442, 2012

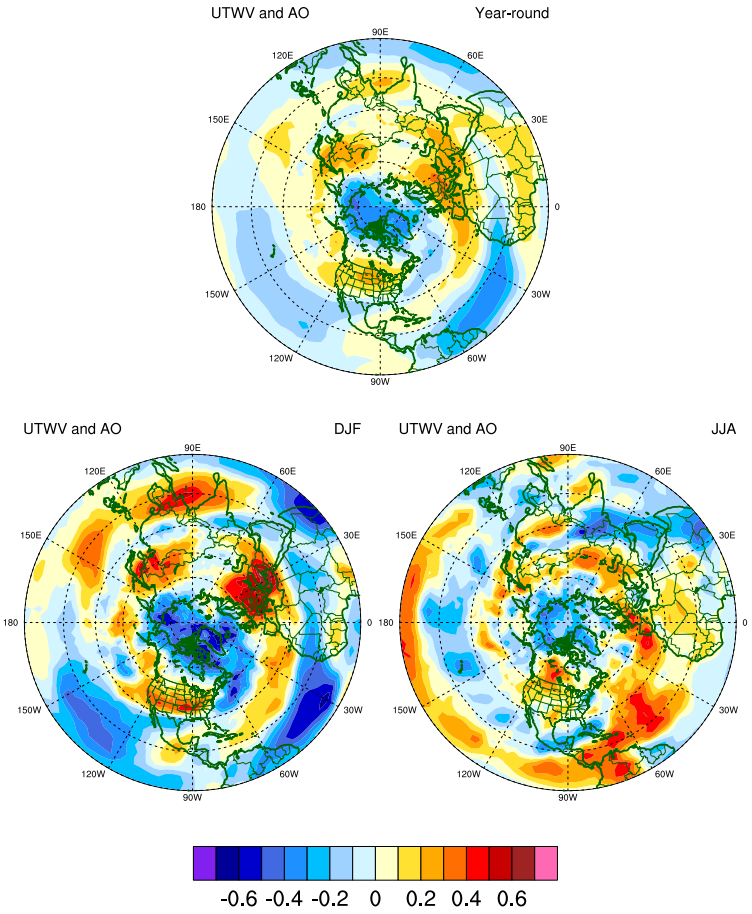

Fig. 9. Correlations between UTWV brightness temperature and AO index for year-round, DJF, and JJA.

ACPD
12, 33411–33442, 2012

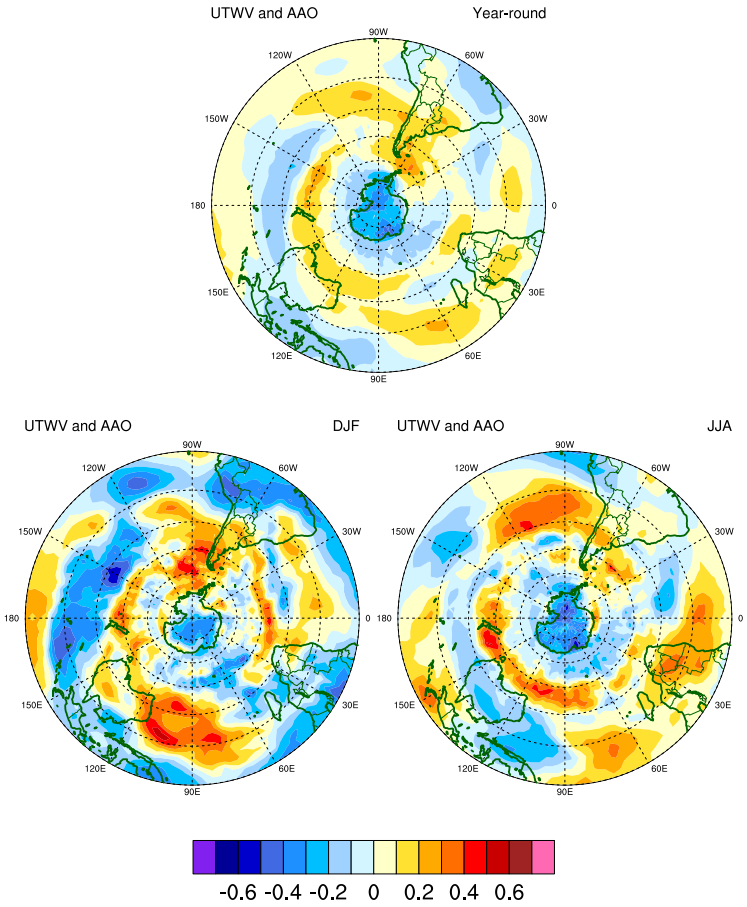

Fig. 10. Correlations between UTWV brightness temperature and AAO index for year-round, DJF, and JJA.

ACPD
12, 33411–33442, 2012